Nano Research
2024, 17(12): 10355–10362

ISSN 1998-0124 CN 11-5974/O4
https://doi.org/10.1007/s12274-024-6950-5

Research Article

Unveiling multimodal hot carrier excitation in plasmonic bimetallic Au@Ag nanostars for photochemistry and SERS sensing

Yoel Negrín-Montecelo[1,§], Amir Elsaidy[2,§], Jesús Giráldez-Martínez[3], Enrique Carbó-Argibay[4], Zhiming Wang[5], Alexander O. Govorov[6] (✉), Ramon A. Alvarez-Puebla[1,7] (✉), Miguel A. Correa-Duarte[3,8] (✉), and Lucas V. Besteiro[3] (✉)

[1] *Department of Physical and Inorganic Chemistry, Universitat Rovira i Virgili, Carrer de Marcel·lí Domingo s/n, Tarragona 43007, Spain*
[2] *Department of chemical engineering, Military Technichal College, Cairo 4393010, Egypt*
[3] *CINBIO, University of Vigo, Campus Universitario de Vigo, Lagoas Marcosende, Vigo 36310, Spain*
[4] *International Iberian Nanotechnology Laboratory, Av. Mestre José Veiga s/n, Braga 4715-330, Portugal*
[5] *Institute of Fundamental and Frontier Sciences, University of Electronic Science and Technology of China, Chengdu 610054, China*
[6] *Department of Physics and Astronomy, Ohio University, Athens, Ohio 45701, USA*
[7] *ICREA, Passeig Lluís Companys 23, Barcelona 08010, Spain*
[8] *Southern Galicia Institute of Health Research (IISGS) and Biomedical Research Networking Center for Mental Health (CIBERSAM), Universidade de Vigo, Vigo 36310, Spain*
[§] *Yoel Negrín-Montecelo and Amir Elsaidy contributed equally to this work.*

Received: 3 June 2024 / **Revised:** 27 July 2024 / **Accepted:** 8 August 2024

ABSTRACT

Plasmonic nanostructures stand at the forefront of nanophotonics research, particularly in sensing and energy conversion applications. Their unique ability to confine light energy at the nanoscale makes them indispensable for a wide array of technological advancements. The study of these structures often makes use of different materials and, even more extensively, explores new shapes and configurations to extend our common repertoire of useful nanophotonics tools. Exploring the creation of bimetallic plasmonic nanostructures combines these two dimensions determining the space of possible plasmonic resonators and opens the possibility of tailoring systems with behavior unavailable to single-metal plasmonic structures. In this paper, we delve into the exploration of bimetallic systems employing plasmonic nanostars. These structures have demonstrated remarkable capabilities for surface-enhanced Raman scattering (SERS) spectroscopy and photochemistry, due to the strong plasmonic response of their peaks, whose disposition following a spherical symmetry makes them largely polarization- and orientation-insensitive. Herein, we report the colloidal synthesis of two different water-stable Au@Ag nanostars, explore their performance as photocatalysts and SERS substrates, and provide an in-depth account of their non-trivial physical response.

KEYWORDS

hot-electrons, field enhancement, nanohybrids, photocatalysis, surface-enhanced Raman scattering (SERS), plasmonics

1 Introduction

The application of plasmonic nanostructures to improve the state of the art in photocatalysis is a particularly active pursuit, on account of the potential of these optically resonant materials to photosensitize wide-band semiconductor photocatalysts or catalytic metals [1, 2], or affect the product selectivity in photocatalytic reactions [3, 4]. In the last decade, nanocomposites assembled using titanium dioxide (TiO_2) and plasmonic nanoparticles (NPs) as building blocks have become interesting materials for the development of new photocatalytic hybrids. NPs-TiO_2 nanocomposites have been used in different environmental and energy fields such as, degradation of organic pollutants [5, 6], water splitting [7, 8], nitrogen photofixation and conversion of CO_2 to hydrocarbon fuels [9, 10]. One of the mechanisms by which plasmonic NPs can affect the course of the reaction is by injecting highly energetic charge carriers excited in the metal [11, 12]. These can drive chemical transformations at the surface of the plasmonic NPs, or transfer these carriers to the TiO_2 [13, 14], whose valence and conduction bands are well-aligned to several reactions of energy interest, including water-splitting and its consequent generation of reactive oxygen species (ROS) [15, 16]. Not less important for mechanisms in delivering the energy in the plasmonic modes to the NPs' environment are the enhancement of optical phenomena through their strong near-fields [17–20], and the increase of local temperature through the photoheating caused by the dissipation of the energy in electronic degrees of freedom through their interaction with the lattice's phonons [21–23].

An additional reason why plasmonic NPs are interesting in nanophotonics, and in solar energy harvesting, is that their optical, and overall physical properties can be plied substantially through changing their material composition and geometry. These two dimensions configure a rich design space for plasmonic NPs.

Address correspondence to Alexander O. Govorov, govorov@ohio.edu; Ramon A. Alvarez-Puebla, ramon.alvarez@urv.cat; Miguel A. Correa-Duarte, macorrea@uvigo.es; Lucas V. Besteiro, lucas.v.besteiro@uvigo.es

There is a significant variety of metal and non-metal plasmonic materials of interest, but "traditional" plasmonic noble metals still retain untapped potential, especially, as we will discuss, when considering multimetallic configurations. AuNPs are widely applied in the assembly of metal-semiconductor nanocomposites thanks to their high biocompatibility, easy surface modification and chemical stability [24–26]. Thanks to its strong optical response and lower cost, AgNPs offers extra advantages in fields such as electron transport, surface-enhanced Raman scattering (SERS) spectroscopy or plasmonic sensing [27, 28]. AgNPs also exhibit a higher electric field enhancements and stronger plasmonic resonances that, together with the limited interband damping effect, ensures elevated hot-electron injection rates and improved photosensitization of the semiconductor in nanorods-TiO_2 composites [29]. Although the synthesis of monometallic anisotropic AgNPs with localized surface plasmon resonance (LSPR) absorption peaks in the visible-near infrared (NIR) interval have been widely applied, the preparation of pure anisotropic forms like stars or rods with sizes under 80 nm has been challenging [30]. In the context of photocatalysis, geometries with abundant and strong hot electromagnetic hot spots, such as nanostars (NSt), offer great promise for carving a path towards larger yields for a given amount of metal [31, 32].

Herein, the behavior of bimetallic gold@silver nanostars (Au@AgNSt) is studied, to map the potential of these hybrid systems in photocatalysis and sensing, expanding on prior explorations of Au@Ag bimetallic rods in such contexts [29, 33, 34]. Two types of Au@AgNSt were prepared through the growth of a homogeneous Ag shell using AuNSt as templates. By assembling the different NSt into a $SiO_2@TiO_2$-NPs composite, both experimental and theoretical studies were conducted to examine the role of morphology and composition in the photosensitizing capabilities of these hybrids. These results were correlated with the experimental photocatalytic and SERS sensitivity behavior of each hybrid under different light illuminations to elucidate the relative importance of their corresponding electromagnetic field enhancements and hot electron (HE) excitation rates in TiO_2 photosensitization.

2 Results and discussion

AuNSt with cores of 35 (± 4) nm, spikes of 9 (± 2) nm (Fig. 1(a),

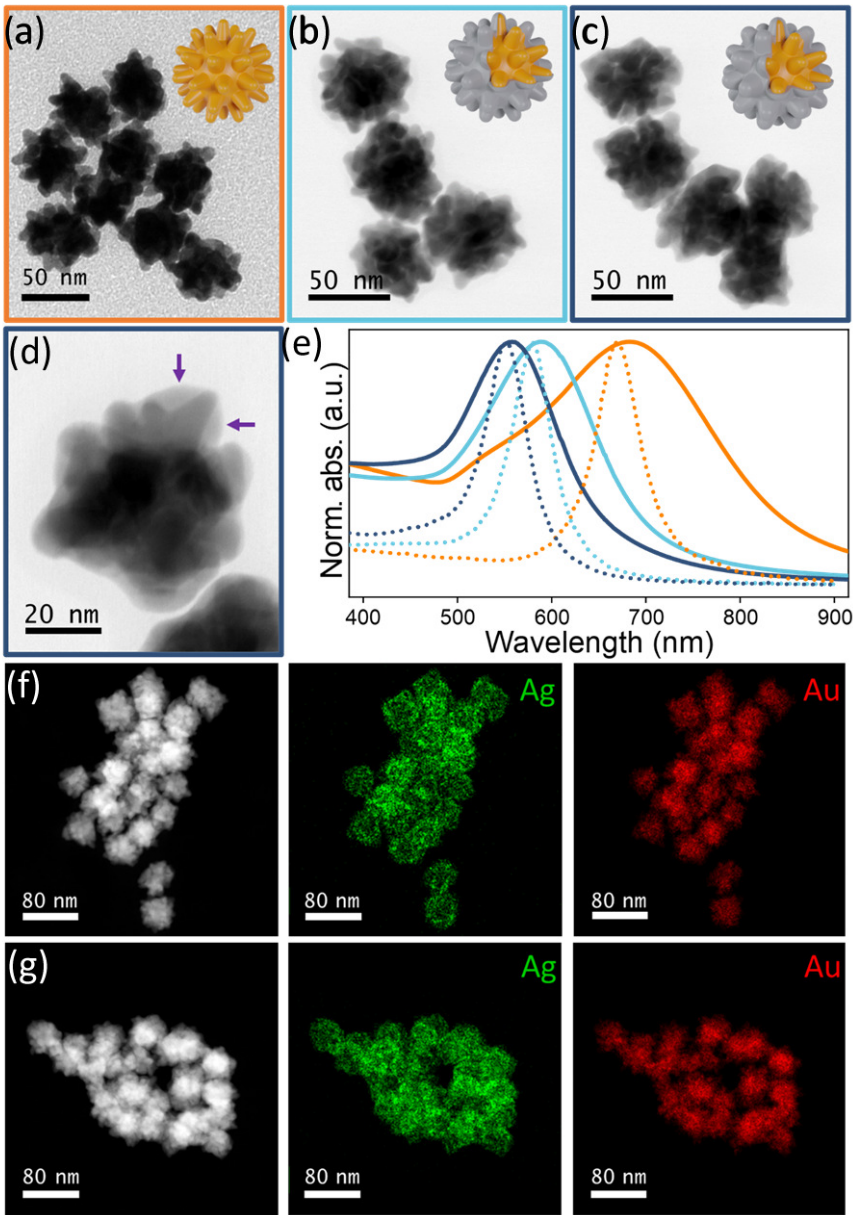

Figure 1 (a) Transmission electron microscopy (TEM) images of AuNSt. High-resolution TEM (HR-TEM) images of (b) Au@Ag1 and ((c) and (d)) Au@Ag2. (e) Experimental (solid) and theoretical (dotted) extinction spectra of AuNSt (orange), Au@Ag1 (light blue) and Au@Ag2 (dark blue). Scanning transmission electron microscopy (STEM) images and EDX mappings for (f) Au@Ag1 and (g) Au@Ag2.

and Figs. S1(a) and S1(d) in the Electronic Supplementary Material (ESM)) and plasmon signature centered in 684 (orange spectra, Fig. 1(e)) were prepared according to a procedure previously reported [32]. Subsequently, the synthetized AuNSt were used as a template for the synthesis of two types of Au@Ag NSt by growing a different thickness of silver [35]. Thus, we prepare Au@Ag1 with 40 (± 4) nm of core and 8 (± 2) nm of spikes (Fig. 1(b), and Figs. S1(b) and S1(e) in the ESM) and Au@Ag2 with 45 (± 5) nm of core and 6 (± 2) nm of spikes (Fig. 1(c), and Figs. S1(c) and S1(f) in the ESM). Interestingly, when the amount of silver is increased the growth takes place preferentially among the Au spikes and we observe more rounded morphologies (Fig. 1(d)). The star shape was reshaped with thicker and shorter tips as we observed in another branched Au@Ag nanoparticles [34]. Nevertheless, both core–shell nanoparticles have a strong plasmonic signatures centered in 588 for the of Au@Ag1 and in 558 nm for Au@Ag2 NSt (light and dark blue lines, respectively, Fig. 1(e)). Computational models of these NSt were created (inserts in Figs. 1(a)–1(c)) and their simulated extinction spectra shows good agreement with the experimental results (dotted spectra, Fig. 1(e)). Additional computational results for pure Ag NSt, shown in Fig. S2 in the ESM, illustrate the blue-shift effect of changing the aspect ratio of the NSt tips when adding the outer Ag layer. The energy-dispersive X-ray spectroscopy (EDX) mappings for Au@Ag1 (Fig. 1(f)) and for Au@Ag2 (Fig. 1(g)) show a homogeneous distribution of the Ag shell.

The photocatalytic efficiency of the synthetized nanocomposites has been evaluated through the photodegradation of Rhodamine B (RhB) as a model reaction. The photocatalytic efficiency of the synthesized nanocomposites (see Figs. 2(a) and 2(c)–2(e)) has been evaluated through the photodegradation of RhB as a model reaction. The degradation of RhB occurs by means of hydroxyl radicals produced by the interaction of holes with the H_2O molecules, demethylating RhB to form Rh110 [16]. In this manner, the photo-oxidation of this dye in the presence of the hybrids was monitored by following the decrease in the absorption maximum of a RhB (λ = 554 nm) as a function of time, using a solar simulator with fiber optic coupling with irradiation of λ = 350–2400 nm (Fig. S4 in the ESM). As a control experiment, silica spheres functionalized only with TiO_2 NPs was used as a catalyst and a 25.4% of degradation of RhB is observed after 5 h of reaction (black circles, Fig. 3(a)) as a result of the direct photoexcitation of the semiconductor with the small fraction of UV photons. When the experiment was carried out using the TiO_2 NPs in contact with the AuNSt we observed an increased degradation of the dye (93.8%) after the same irradiation time (orange circles, Fig. 3(a)). Interestingly, when the silver-coated nanostars are used a loss in the photocatalytic efficiency of the hybrids is observed (63.9% and 53.1% for Au@Ag1 and Au@Ag2, light and dark blue circles, respectively, Figs. 3(a) and 3(b)). These results are somewhat surprising, as often silver nanostructures offer a stronger photocatalytic effect than that of gold [27, 30], and previous experimental and theoretical results point towards using Au@Ag nanostructures as enhanced photocatalysts [29, 33]. These new results therefore highlight that such strategy is strongly geometry-dependent, and merit an in-depth analysis supported by a detailed characterization of these plasmonic systems.

In order to evaluate the photosensitizing capabilities of the prepared NSt we integrate them into hybrid photocatalysts. For this purpose, 500 nm silica beads exposed to a positively-charged solution of polyelectrolyte have been used as supports for the adsorption of a layer of 5 nm TiO_2 nanoparticles and the NSt functionalized with a negatively charged polyelectrolyte (Fig. 2(a)). This layer-by-layer protocol (LbL) has been previously used for the assembly of plasmonic nanoparticles (PNPs) and semiconductors permitting a tight control in the composition and functionality of the final structure [29]. Moreover, the $SiO_2@TiO_2@NSt$ hybrids formed in this way present the same PNP/TiO_2 molar ratio (0.12), high homogeneity and colloidal

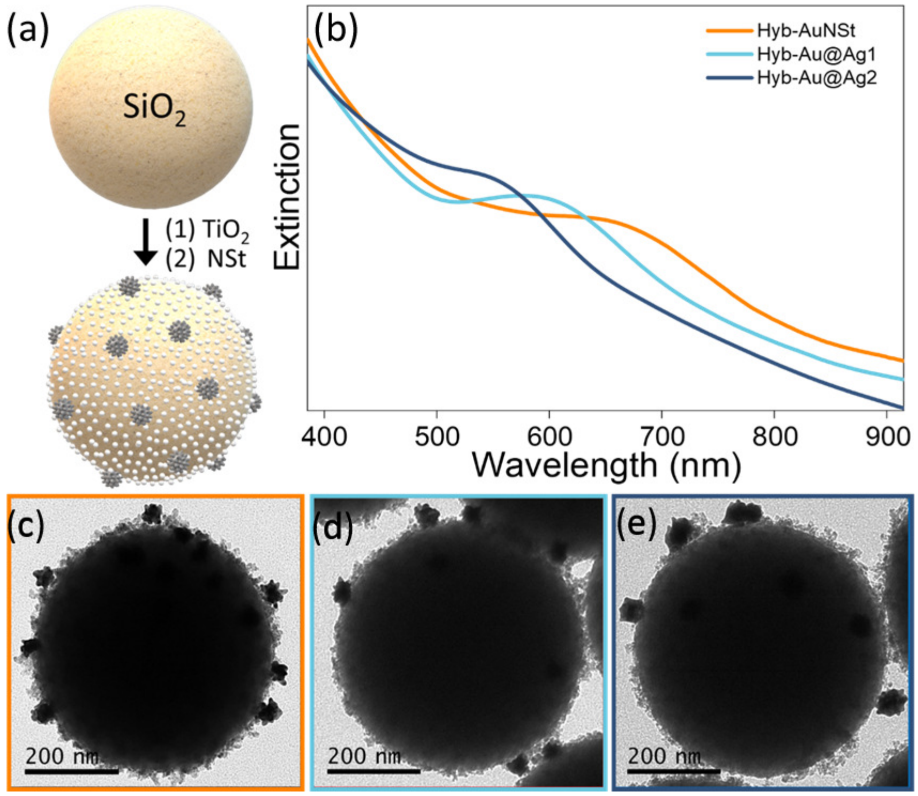

Figure 2 (a) Scheme of the layer-by-layer assembly of the hybrid photocatalysts. In a first step, TiO_2 NPs are adsorbed onto SiO_2 spheres and, subsequently, the chosen NSt is added. (b) Extinction spectra of hybrid photocatalysts formed with AuNSt (orange), Au@Ag1 (light blue) and Au@Ag2 (blue). (c)–(e) TEM images of the hybrid photocatalysts formed with AuNSt, Au@Ag1 and Au@Ag2, respectively.

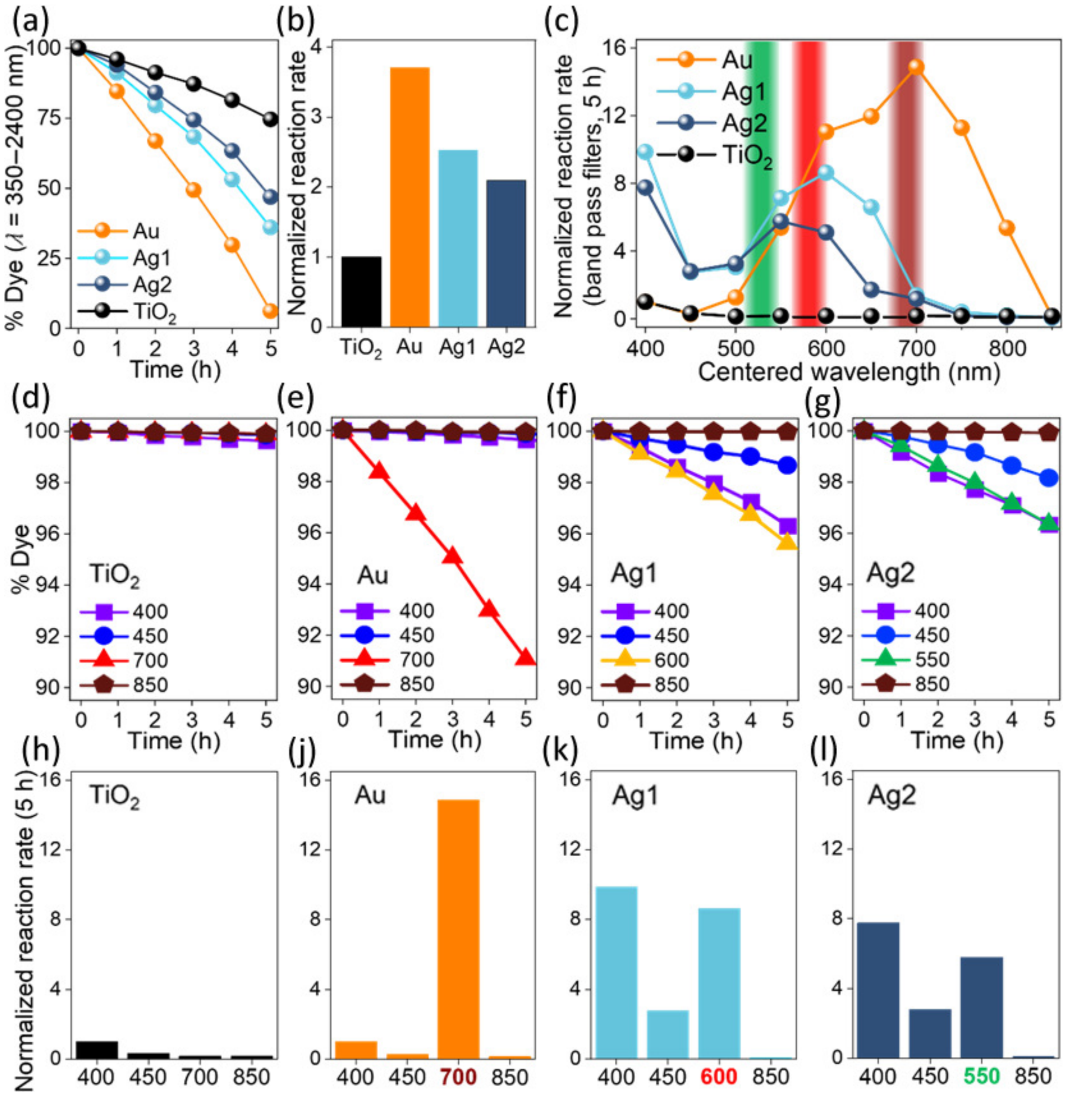

Figure 3 (a) Photocatalytic activity profiles and (b) normalized reaction rates of the catalysts when the solution was exciting with wavelength from 350 to 2400 nm after 5 h of irradiation. (c) Rate of degradation of RhB after 5 h of illumination using the bandpass filters normalized by the area of the transmission spectra of each filter (see Fig. S5 in the ESM). (d)–(g) Photocatalytic activity profiles of the hybrid using the 40 nm bandpass filters at 400, 450, 850 nm and at the λ_{max} of the absorption spectra for each catalyst. (h)–(k) Normalized reaction rate in the degradation of RhB using the filters of reference and with the filter that cover the λ_{max} of the absorption spectra for each catalyst. The reaction rates in panels (c) and (h)–(k) are normalized by the amount of degradation achieved by TiO_2 under 400 nm light. The results are presented with a color code depending on the photocatalysts, with TiO_2 alone, AuNSt, Au@Ag1 and Au@Ag2 represented in black, orange, light blue and dark blue, respectively. The photocatalysis is conducted at 1 atm and 25 °C for 5 h.

stability (Figs. 2(c)–2(e) and Figs. S3(a)–S3(c) in the ESM). Regarding the optical properties, the hybrids display a strong extinction at short wavelengths as a consequence of the TiO_2 absorption in the UV region and a pronounced scattering contribution from the SiO_2 beads (Fig. 2(b)), with a long tail covering the full visible spectrum. The LSPR signatures of the different NSt are nonetheless still discernible, with the expected small red shift due to the increased effective refractive index around the plasmonic NSt from the SiO_2 and TiO_2.

Let us start the analysis of these photocatalysts by disentangling the spectral response of the hybrid photocatalytic systems, exploring which plasmonic modes are contributing to the overall activity. For this, the degradation of RhB was performed using bandpass filters, with a spectral width of 40 nm, with wavelengths centered every 50 nm from 400 to 850 nm (Figs. S4–S6 in the ESM). The spectral degradation profiles are shown in Fig. 3(c), weighted by the transmission of each filter and taking as normalized to reference degradation of TiO_2 at 400 nm. Interestingly, we see additional features in these spectra beyond those in the absorbance of the NSt (Fig. 1(e)) and, importantly, we also find that the main plasmonic mode of the Au@AgNSt is significantly less efficient than that of the AuNSt. The maximum degradation of the organic dye in the main plasmonic mode was reached using the 700 nm filter for AuNSt, the 600 nm filter for Au@Ag1 and the 550 nm filter for Au@Ag2 (achieving 14.88%, 8.63% and 5.76% degradation after 5 h, respectively. Fig. 3(c)). Additionally, we see that the Au@AgNSt degrade the RhB notably well at shorter wavelengths, even surpassing the efficiency at the main peak at 400 nm. Note that this occurs at wavelengths for which we see no clear evidence of a plasmonic mode in the optical spectra (refer again to Fig. 1(d)), and coincide with the wavelengths in which the TiO_2 is directly contributing to the photodegradation (see Fig. 3(c), black points). In Figs. 3(d)–3(g) we show absolute degradation percentages for each catalyst to see the kinetics leading to the results above. Please note that each of these panels highlight notable wavelengths for each catalyst, and the main plasmonic mode is different between Figs. 3(d)–3(g). We observe the fastest degradation in the case of AuNSt at 700 nm (red line, Fig. 3(e)) with almost the double of degradation rate compared with Au@Ag1 and Au@Ag2 at 600 and 550 nm (yellow and green lines in Figs. 3(f) and 3(g), respectively). In the case of exciting the catalyst with AuNSt at shorter wavelengths (filters at

400 and 450 nm) the contribution of the plasmonics nanoparticles to the TiO_2 photoactivation are practically null (Figs. 3(h) and 3(i)). Lastly, in Figs. 3(h)–3(k) we summarize the normalized reaction rates for wavelengths selected in the previous panels, which highlight the relevant relative magnitudes of the different spectral contributions and the distinct behavior between AuNSt and Au@AgNSt. At this point, the photodegradation spectra for Au@AgNSt shows that their overall contribution, smaller than that of AuNSt, is divided between two modes, the second of which can arise through the Ag-mediated enhancement of absorption in the TiO_2. However, we will argue that, although present, this is not the dominant mechanism creating these short-wavelength photodegradation modes, but the photogeneration of hot carrier at the Ag surface. Is also important to note that photocatalytic experiments were performed with a sample in a thermal bath at a fixed temperature of 25 °C, so that temperature-driven photocatalysis was ruled out as a relevant contribution to the overall effect [15].

SERS characterization was employed to deepen our understanding of the contributions of the metal NSt to the optical excitation of nearby species through near-field interaction (Fig. 4). Enhanced Raman was collected with three laser lines at 514, 633., and 785 nm, respectively, as highlighted in Fig. 3(c). Figures 4(a)–4(c) show the absorption and emission spectra of RhB, the SERS/surface-enhanced resonance Raman scattering (SERRS) spectra of the molecule upon excitation with each of the laser lines and the (normalized and absolute) intensities obtained with each of the nanostars at the different excitation lights.

Initially focusing on the curve for AuNSt, it exhibits a clear growth as the wavelength increases, with the most significant enhancement occurring near the long-wavelength dipolar plasmonic mode of the NSt. At this wavelength, the Au@AgNSt contribution to the SERS signal is modest. Interestingly, the signal obtained at 633 nm from the AuNSt sample falls below that of both Au@AgNSt, as we are now closer to the main resonances of these latter bimetallic structures. Furthermore, at 514 nm, the AuNSt do not contribute to the SERS intensity due to Au interband excitation [27]. However, the Ag-coated NSt provide a much larger signal at this wavelength, attributed to several factors: the absence of interband transitions in Ag at these energies, the field enhancement of the Au@AgNSt plasmonic modes, and the presence of a strong absorption line of RhB. Hence, it becomes evident that we are observing doubly resonant phenomena, i.e., SERRS [36].

To further disentangle the effect of the plasmonic near-field and the resonant charge transfer to RhB, we have also characterized these NSt using benzenethiol as a SERS reporter. Benzenethiol was chosen because neither its absorption nor emission overlaps with the plasmonic modes of the NSt (see Fig. 4(d)), and the signal is solely attributable to the exchange of virtual photons [37]. In this case, the collected SERS intensity spectra in Fig. 4(f) are clearly dominated by the strong dipolar plasmon in Au, with the mixed bimetallic plasmonic modes of the Au@AgNSt offering a much weaker contribution. Additionally, in the normalized data shown in Fig. 4(e), a clearer correlation between these SERS datasets and the spectra of the plasmonic modes (Fig. 1(e)) can be observed.

It is now apparent that in Figs. 4(b) and 4(c), the resonant (514 nm) and pre-resonant (633 nm) optical excitation of RhB with the Au@AgNSt is observed. This mechanism leads to photobleaching, suggesting its contribution to the overall photodegradation effect (Fig. 3) observed using the hybrid photocatalysts (Fig. 2) for wavelengths overlapping with the RhB absorption spectrum. However, as the relative strengths between AuNSt and Au@AgNSt in Fig. 4(c) at these wavelengths are not preserved in the spectrally-resolved photodegradation results (Fig. 3(c)), this is not the dominant mechanism in the overall photodegradation. The injection of plasmonic intraband hot carriers is more likely to be the dominant photodegradation mechanism, mediated by their injection into TiO_2 nanoparticles and the subsequent generation of reactive oxygen species [38, 39]. Additionally, since none of the NSt exhibit a clear plasmonic mode around wavelengths of 400 nm (Fig. 1(e)), plasmonic enhancement of TiO_2 optical excitation is unlikely to significantly contribute to RhB photodegradation.

Finally, we perform theoretical simulations to explore the detailed response of these NSt and contrast them against the different experimental data and characterization. The electrodynamic simulations were performed with COMSOL, and the hot carrier excitation was modelled using a semiclassical formalism accounting for the quantum effects allowing optical transitions at the metal surface. Details of the computational technique and physical model can be found in the ESM. The

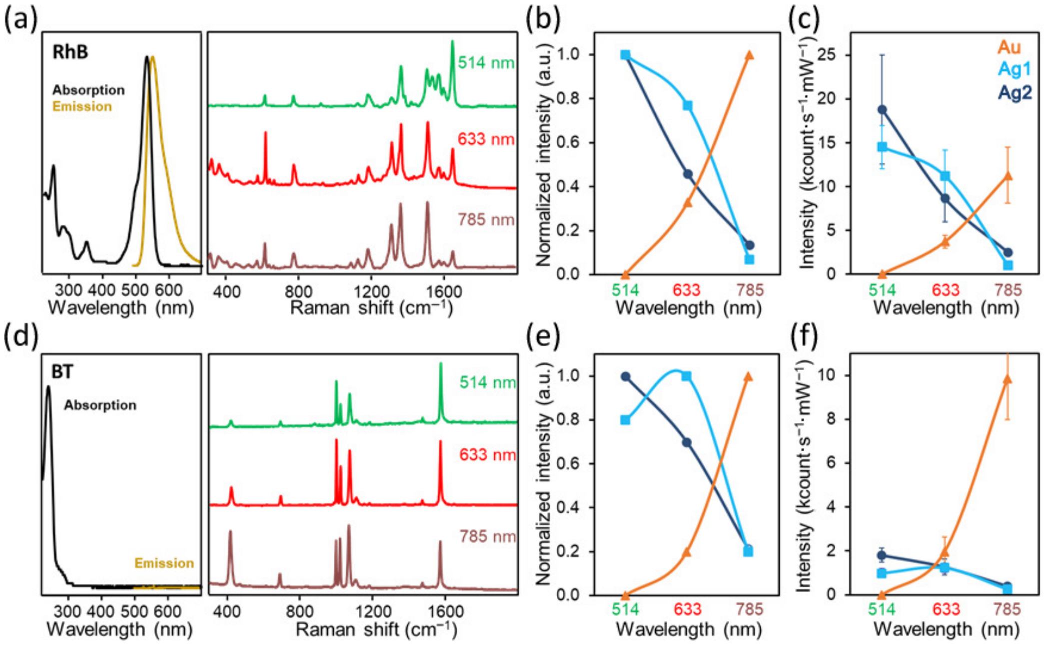

Figure 4 UV–Vis and SERS/SERRS characterization of the NSt using RhB and benzenethiol (BT) as analytes. Absorption, emission, and Raman spectra of (a) RhB and (d) BT. (b) and (e) Normalized and (c) and (f) absolute SERS/SERRS signal intensity, at 1355 cm^{-1} for RhB and at 999 cm^{-1} for BT, respectively, using our three different metal NSt (common legend in panel c) and under three different wavelengths.

geometries of the three types of NSt were created to match the general geometry seen in the TEM images, with larger spherical symmetry to create more general models, and the ultraviolet–visible (UV–Vis) spectroscopy data. The three-dimensional (3D) models in Figs. 1(a)–1(c) represent these geometries, and the dashed spectra in Fig. 1(e) are the normalized extinction cross-sections from the simulations. We can find the central computational results in Fig. 5, with panel a showing the spectra of rate HE, the computed rates of excitation of intraband hot carriers at the interfaces between metal and environment. These rates for the excitation of electron and holes with excess energy were computed using a semiclassical formalism accounting for the optical transitions allowed by the symmetry-breaking of the NP surfaces (additional details in the ESM and Refs. [40, 41].

$$\mathrm{FE} = |\mathbf{E}(\mathbf{r})|^2 / E_0^2$$

where $\mathbf{E}(\mathbf{r})$ is the electric field at point $\mathbf{r}$ and E_0 is the electric field's amplitude of the planewave impinging on the nanostructure. Figure 5(c) shows the spectra for this magnitude, averaged over a small volume surrounding the NSt' surface. These data show the enhancement at the plasmonic mode of the NSt, with lower peak values for the Ag-coated systems. The dashed line in Fig. 5(c) marks the wavelength corresponding to the main absorption peak of RhB, at 525 nm (see Fig. 4(a)), which partially overlaps with the Au@AgNSt modes. From these results we could expect a plasmonic enhancement of RhB's optical absorption only by the bimetallic stars and in an amount that increases with the thickness of deposited Ag, in correspondence with our SERS results (Fig. 4(c)). On the other hand, the enhancement at shorter wavelengths is small for the Au@AgNSt, negligible for the AuNSt, and with no discernable spectral features, suggesting that the plasmonic NSt enhancement of the absorption in the $\mathrm{TiO_2}$ NPs is not a major contributor to the photodegradation observed experimentally. Figures 5(d)–5(f) show FE maps at the surface of the NSt and on a transversal cross section of the space surrounding them, under 525 nm light. These maps were obtained for a single polarization of the incoming light, thus showcasing a lateral charge separation in the chosen perspective, being clearest for the Au@Ag2NSt in Fig. 5(f) because at this wavelength we are closest to its plasmonic mode. This is also evident from the larger FE values seen for this structure. Field enhancement maps for other significant wavelengths can be found in Fig. S8 in the ESM.

3 Conclusion

Bimetallic Au@AgNSt were prepareded using AuNSt as a template and tested as photosensitizers in hybrid photocatalytic systems, using RhB degradation as a model reaction. Using a combination of SERS, with both RhB and benzenethiol as Raman reporters, and computational characterization of the nanostars, it was shown that the dominant driver of photodegradation is most likely the injection of hot carriers from the plasmonic structures. Characterization revealed the presence of a secondary mode in the excitation of plasmonic intraband hot carriers at the Ag surface, which was not expected by simply examining the optical response of the bimetallic nanostars. Jointly, the photodegradation and characterization results highlight that creating multimetallic plasmonic structures with complex geometries can yield novel and interesting behavior, emphasizing the interest in exploring comparatively unexplored design spaces.

Acknowledgements

This work was supported by the projects PID2020-120306RB-I00, PID2020-118282RA-I00, PID2020-113704RB-I00; TED2021-130038A-I00, TED2021-132101B-I00, RYC2021-033818-I, PDC2021-121787-I00, and FPU21/03137, funded by MCIN/AEI/10.13039/501100011033 and European Union "NextGenerationEU"/PRTR; ED431C 2022/24 funded by Xunta de Galicia; 2020SGR00166 funded by Generalitat de Cataluña; 2021PFR-URV-B2-02 funded by Universitat Rovira i Virgili; HORIZON-EIC-2022-PATHFINDERCHALLENGES-01-06 (No. 101115149), HORIZON-HLTH-2022-DISEASE-06-TWO-STAGE (No. 101080889), funded by the European Union Horizon 2020 Research and Innovation Program. This work was carried out in part through the use of the INL Research Core Facilities

Funding note: Open Access funding provided thanks to the CRUE-CSIC agreement with Springer Nature.

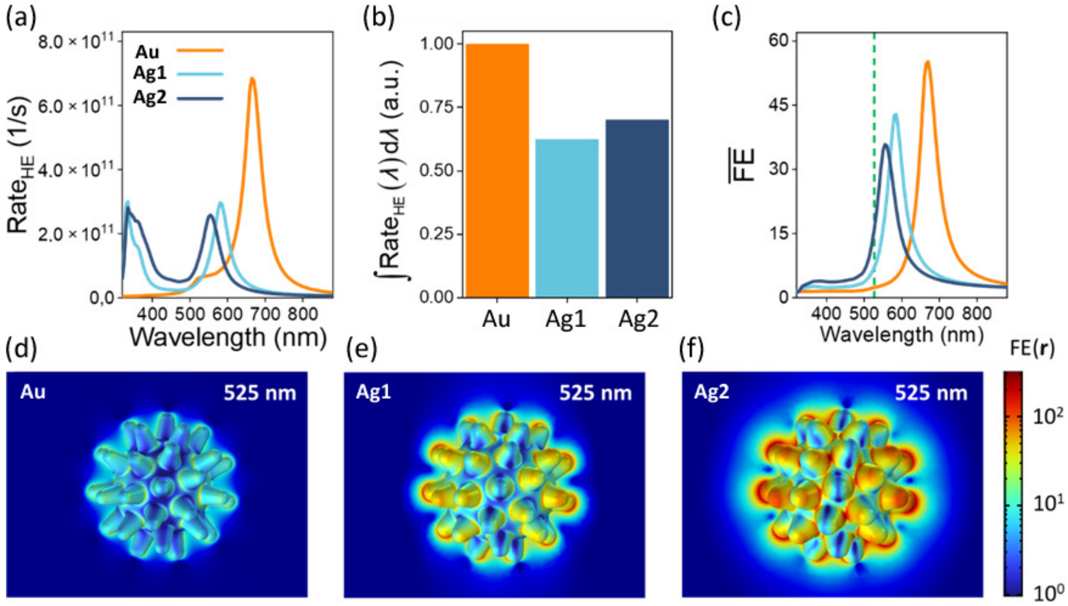

Figure 5 (a) Rate of excitation of intraband hot carriers for the three systems and (b) integrated values under these curves (normalized to the value for AuNSt), estimating the relative total rates of hot carrier excitation for each NSt under a broadband source with a flat spectrum. (c) Volume-averaged field enhancement around the surface of the metal. We highlight the approximate wavelength of excitation of the RhB molecules. (d)–(f) FE maps around the metal NSs. We show the values at the surface of the NS, together with a transversal cross-section of the space around them.

Electronic Supplementary Material: Supplementary material (detailed methodology, NSt size histograms, additional TEM images, photocatalysis setup, filter spectra, detailed degradation data, and additional computational results) is available in the online version of this article at https://doi.org/10.1007/s12274-024-6950-5.

References

[1] Linic, S.; Christopher, P.; Ingram, D. B. Plasmonic-metal nanostructures for efficient conversion of solar to chemical energy. *Nat. Mater.* **2011**, *10*, 911–921.

[2] Sytwu, K.; Vadai, M.; Dionne, J. A. Bimetallic nanostructures: Combining plasmonic and catalytic metals for photocatalysis. *Adv. Phys.: X* **2019**, *4*, 1619480.

[3] Li, Z. D.; Ehtesabi, S.; Gojare, S.; Richter, M.; Kupfer, S.; Gräfe, S.; Kurouski, D. Plasmon-determined selectivity in photocatalytic transformations on gold and gold-palladium nanostructures. *ACS Photonics* **2023**, *10*, 3390–3400.

[4] Creel, E. B.; Corson, E. R.; Eichhorn, J.; Kostecki, R.; Urban, J. J.; McCloskey, B. D. Directing selectivity of electrochemical carbon dioxide reduction using plasmonics. *ACS Energy Lett.* **2019**, *4*, 1098–1105.

[5] Anjugam Vandarkuzhali, S. A.; Pugazhenthiran, N.; Mangalaraja, R. V.; Sathishkumar, P.; Viswanathan, B.; Anandan, S. Ultrasmall plasmonic nanoparticles decorated hierarchical mesoporous TiO_2 as an efficient photocatalyst for photocatalytic degradation of textile dyes. *ACS Omega* **2018**, *3*, 9834–9845.

[6] Zada, A.; Qu, Y.; Ali, S.; Sun, N.; Lu, H. W.; Yan, R.; Zhang, X. L.; Jing, L. Q. Improved visible-light activities for degrading pollutants on TiO_2/g-C_3N_4 nanocomposites by decorating SPR Au nanoparticles and 2, 4-dichlorophenol decomposition path. *J. Hazard. Mater.* **2018**, *342*, 715–723.

[7] Liu, Z. W.; Hou, W. B.; Pavaskar, P.; Aykol, M.; Cronin, S. B. Plasmon resonant enhancement of photocatalytic water splitting under visible illumination. *Nano Lett.* **2011**, *11*, 1111–1116.

[8] Chen, J. J.; Wu, J. C. S.; Wu, P. C.; Tsai, D. P. Plasmonic photocatalyst for H_2 evolution in photocatalytic water splitting. *J. Phys. Chem. C* **2011**, *115*, 210–216.

[9] J. H.; Guo, Y. Z.; Jiang, R. B.; Qin, F.; Zhang, H.; Lu, W. Z.; Wang, J. F.; Yu, J. C. High-efficiency "working-in-tandem" nitrogen photofixation achieved by assembling plasmonic gold nanocrystals on ultrathin titania nanosheets. *J. Am. Chem. Soc.* **2018**, *140*, 8497–8508.

[10] Hou, W. B.; Hung, W. H.; Pavaskar, P.; Goeppert, A.; Aykol, M.; Cronin, S. B. Photocatalytic conversion of CO_2 to hydrocarbon fuels via plasmon-enhanced absorption and metallic interband transitions. *ACS Catal.* **2011**, *1*, 929–936.

[11] Hartland, G. V.; Besteiro, L. V.; Johns, P.; Govorov, A. O. What's so hot about electrons in metal nanoparticles. *ACS Energy Lett.* **2017**, *2*, 1641–1653.

[12] Kale, M. J.; Avanesian, T.; Christopher, P. Direct photocatalysis by plasmonic nanostructures. *ACS Catal.* **2014**, *4*, 116–128.

[13] Sousa-Castillo, A.; Comesaña-Hermo, M.; Rodríguez-González, B.; Pérez-Lorenzo, M.; Wang, Z. M.; Kong, X. T.; Govorov, A. O.; Correa-Duarte, M. A. Boosting hot electron-driven photocatalysis through anisotropic plasmonic nanoparticles with hot spots in Au-TiO_2 nanoarchitectures. *J. Phys. Chem. C* **2016**, *120*, 11690–11699.

[14] Gosciniak, J.; Atar, F. B.; Corbett, B.; Rasras, M. Plasmonic Schottky photodetector with metal stripe embedded into semiconductor and with a CMOS-compatible titanium nitride. *Sci. Rep.* **2019**, *9*, 6048.

[15] Negrín-Montecelo, Y.; Brissaud, C.; Piquemal, J. Y.; Govorov, A. O.; Correa-Duarte, M. A.; Besteiro, L. V.; Comesaña-Hermo, M. Plasmonic photocatalysis in aqueous solution: Assessing the contribution of thermal effects and evaluating the role of photogenerated ROS. *Nanoscale* **2022**, *14*, 11612–11618.

[16] Sousa-Castillo, A.; Couceiro, J. R.; Tomás-Gamasa, M.; Mariño-López, A.; López, F.; Baaziz, W.; Ersen, O.; Comesaña-Hermo, M.; Mascareñas, J. L.; Correa-Duarte, M. A. Remote activation of hollow nanoreactors for heterogeneous photocatalysis in biorelevant media. *Nano Lett.* **2020**, *20*, 7068–7076.

[17] Asapu, R.; Claes, N.; Ciocarlan, R. G.; Minjauw, M.; Detavernier, C.; Cool, P.; Bals, S.; Verbruggen, S. W. Electron transfer and near-field mechanisms in plasmonic gold-nanoparticle-modified TiO_2 photocatalytic systems. *ACS Appl. Nano Mater.* **2019**, *2*, 4067–4074.

[18] Hayashido, Y.; Naya, S. I.; Tada, H. Local electric field-enhanced plasmonic photocatalyst: Formation of Ag cluster-incorporated AgBr nanoparticles on TiO_2. *J. Phys. Chem. C* **2016**, *120*, 19663–19669.

[19] T.; Horibe, H.; Kameyama, T.; Okazaki, K. I.; Ikeda, S.; Matsumura, M.; Ishikawa, A.; Ishihara, H. Plasmon-enhanced photocatalytic activity of cadmium sulfide nanoparticle immobilized on silica-coated gold particles. *J. Phys. Chem. Lett.* **2011**, *2*, 2057–2062.

[20] Li, K.; Hogan, N. J.; Kale, M. J.; Halas, N. J.; Nordlander, P.; Christopher, P. Balancing near-field enhancement, absorption, and scattering for effective antenna-reactor plasmonic photocatalysis. *Nano Lett.* **2017**, *17*, 3710–3717.

[21] Govorov, A. O.; Zhang, H.; Demir, H. V.; Gun'ko, Y. K. Photogeneration of hot plasmonic electrons with metal nanocrystals: Quantum description and potential applications. *Nano Today* **2014**, *9*, 85–101.

[22] Baffou, G.; Quidant, R. Thermo-plasmonics: Using metallic nanostructures as nano-sources of heat. *Laser Photonics Rev.* **2013**, *7*, 171–187.

[23] Chang, L.; Besteiro, L. V.; Sun, J. C.; Santiago, E. Y.; Gray, S. K.; Wang, Z. M.; Govorov, A. O. Electronic structure of the plasmons in metal nanocrystals: Fundamental limitations for the energy efficiency of hot electron generation. *ACS Energy Lett.* **2019**, *4*, 2552–2568.

[24] C.; Martínez, R.; Navarro Poupard, M. F.; Pelaz, B.; Polo, E.; Arenas-Vivo, A.; Olgiati, A.; Taboada, P.; Soliman, M. G.; Catalán, Ú. et al. Aqueous stable gold nanostar/ZIF-8 nanocomposites for light-triggered release of active cargo inside living cells. *Angew. Chem., Int. Ed.* **2019**, *58*, 7078–7082.

[25] Alvarez-Puebla, R. A.; Liz-Marzán, L. M. SERS-based diagnosis and biodetection. *Small* **2010**, *6*, 604–610.

[26] Guerrini, L.; Alvarez-Puebla, R. A.; Pazos-Perez, N. Surface modifications of nanoparticles for stability in biological fluids. *Materials* **2018**, *11*, 1154.

[27] Zhao, J.; Pinchuk, A. O.; McMahon, J. M.; Li, S. Z.; Ausman, L. K.; Atkinson, A. L.; Schatz, G. C. Methods for describing the electromagnetic properties of silver and gold nanoparticles. *Acc. Chem. Res.* **2008**, *41*, 1710–1720.

[28] J.; Jimenez de Aberasturi, D.; Aizpurua, J.; Alvarez-Puebla, R. A.; Auguié, B.; Baumberg, J. J.; Bazan, G. C.; Bell, S. E. J.; Boisen, A.; Brolo, A. G. et al. Present and future of surface-enhanced Raman scattering. *ACS Nano* **2020**, *14*, 28–117.

[29] Negrín-Montecelo, Y.; Comesaña-Hermo, M.; Khorashad, L. K.; Sousa-Castillo, A.; Wang, Z. M.; Pérez-Lorenzo, M.; Liedl, T.; Govorov, A. O.; Correa-Duarte, M. A. Photophysical effects behind the efficiency of hot electron injection in plasmon-assisted catalysis: The joint role of morphology and composition. *ACS Energy Lett.* **2020**, *5*, 395–402.

[30] Rycenga, M.; Cobley, C. M.; Zeng, J.; Li, W. Y.; Moran, C. H.; Zhang, Q.; Qin, D.; Xia, Y. N. Controlling the synthesis and

assembly of silver nanostructures for plasmonic applications. *Chem. Rev.* **2011**, *111*, 3669–3712.

[31] Becerril-Castro, I. B.; Calderon, I.; Pazos-Perez, N.; Guerrini, L.; Schulz, F.; Feliu, N.; Chakraborty, I.; Giannini, V.; Parak, W. J.; Alvarez-Puebla, R. A. Gold Nanostars: Synthesis, optical and SERS analytical properties. *Anal. Sens.* **2022**, *2*, e202200005.

[32] L.; Álvarez-Puebla, R. A.; Pastoriza-Santos, I.; Mazzucco, S.; Stéphan, O.; Kociak, M.; Liz-Marzán, L. M.; García de Abajo, F. J. Zeptomol detection through controlled ultrasensitive surface-enhanced Raman scattering. *J. Am. Chem. Soc.* **2009**, *131*, 4616–4618.

[33] Muravitskaya, A.; Movsesyan, A.; Ávalos-Ovando, O.; Bahamondes Lorca, V. A.; Correa-Duarte, M. A.; Besteiro, L. V.; Liedl, T.; Yu, P.; Wang, Z. M.; Markovich, G. et al. Hot electrons and electromagnetic effects in the broadband Au, Ag, and Ag–Au nanocrystals: The UV, visible, and NIR plasmons. *ACS Photonics* **2024**, *11*, 68–84.

[34] Rodríguez-Lorenzo, L.; de la Rica, R.; Álvarez-Puebla, R. A.; Liz-Marzán, L. M.; Stevens, M. M. Plasmonic nanosensors with inverse sensitivity by means of enzyme-guided crystal growth. *Nat. Mater.* **2012**, *11*, 604–607.

[35] Fales, A. M.; Yuan, H.; Vo-Dinh, T. Development of hybrid silver-coated gold nanostars for nonaggregated surface-enhanced Raman scattering. *J. Phys. Chem. C* **2014**, *118*, 3708–3715.

[36] Hildebrandt, P.; Stockburger, M. Surface-enhanced resonance Raman spectroscopy of rhodamine 6G adsorbed on colloidal silver. *J. Phys. Chem.* **1984**, *88*, 5935–5944.

[37] Haynes, C. L.; Van Duyne, R. P. Plasmon-sampled surface-enhanced Raman excitation spectroscopy. *J. Phys. Chem. B* **2003**, *107*, 7426–7433.

[38] Nosaka, Y.; Nosaka, A. Y. Generation and detection of reactive oxygen species in photocatalysis. *Chem. Rev.* **2017**, *117*, 11302–11336.

[39] Zorlu, T.; Becerril-Castro, I. B.; Sousa-Castillo, A.; Puértolas, B.; Besteiro, L. V.; Wang, Z. M.; Govorov, A.; Correa-Duarte, M. A.; Alvarez-Puebla, R. A. Metal-organic frameworks photocatalyst through plasmon-induced hot-electrons. *Adv. Functi. Mater.*, in press, DOI: 10.1002/adfm.202410352.

[40] Juodėnas, M.; Peckus, D.; Tamulevičius, T.; Yamauchi, Y.; Tamulevičius, S.; Henzie, J. Effect of Ag nanocube optomechanical modes on plasmonic surface lattice resonances. *ACS Photonics* **2020**, *7*, 3130–3140.

[41] Santiago, E. Y.; Besteiro, L. V.; Kong, X. T.; Correa-Duarte, M. A.; Wang, Z. M.; Govorov, A. O. Efficiency of hot-electron generation in plasmonic nanocrystals with complex shapes: Surface-induced scattering, hot spots, and interband transitions. *ACS Photonics* **2020**, *7*, 2807–2824.